Electronic Supplementary Material (ESI) for ChemComm.
This journal is © The Royal Society of Chemistry 2023
Please do not adjust margins

Supporting Information

Controllable fabrication of iron-nickle alloy embedded in nitrogen-doped carbon for oxygen evolution

Rong Lin†, Lujiao Mao†, Yi Ding and Jinjie Qian*

Key Laboratory of Carbon Materials of Zhejiang Province, College of Chemistry and Materials Engineering, Wenzhou University, Wenzhou 325035, Zhejiang, P. R. China

†These authors contributed equally to this work.

*Corresponding Author.

E-mail address: jinjieqian@wzu.edu.cn

Please do not adjust margins

Please do not adjust margins

1. Experimental Details

1.1 Reagents and Materials.

All chemicals and solvents are used in this work without further purification 2-Aminoterephthalic acid (NH_2-H_2BDC, AR, > 98.0%, Aladdin), Terephthalic acid (H_2BDC, AR, > 98.0%, Aladdin), Polyvinylpyrrolidone (PVP, 99.0%, 58,000, Aladdin), Zinc nitrate ($Zn(NO_3)_2 \cdot 6H_2O$, AR, 99%, Aladdin), Iron chloride hexahydrate ($FeCl_3 \cdot 6H_2O$, AR, 99%, Aladdin), Nickel(II) acetate tetrahydrate ($Ni(CH_3COO)_2 \cdot 4H_2O$, AR, 99% Aladdin), deionized water (DI H_2O, 18 MΩ), N,N'-dimethyformamide (DMF, ≥99.8%, Aladdin), ethanol (EtOH, >99%, GC, Aladdin) and Nafion (5 wt%, DuPont).

1.2 Syntheses of MOF-5-NH_2 and MOF-5.

Firstly, 250 mg of polyvinylpyrrolidone (PVP, 58,000) was completely dissolved in 10 mL of EtOH:DMF (v:v=1:1) mixture, and then the mixture was heated openly at 130 ℃ for 15 min with stirring speed of 500 rpm. Then, 5 mL of DMF solution containing $Zn(NO_3)_2 \cdot 6H_2O$ (300 mg) and NH_2-H_2BDC (75 mg) was added to the above solution and the reaction was carried out at 130 °C for 2 hours. After cooling to room temperature, the product was collected and centrifuged, washed three times with EtOH, and then the filtered solid was dried under vacuum at 60 ℃ overnight to obtain pure MOF-5-NH_2 in high yield. The preparation of MOF-5 was the same as that of MOF-5-NH_2 except that NH_2-H_2BDC was replaced with H_2BDC.In this work, based on the added organic ligands, the yield of MOF-5-NH_2 is calculated to be ~55%.

1.3 Syntheses of FeNi@NC, FeNi@C and NC.

FeNi@NC was produced by thoroughly grinding 30 mg MOF-5-NH_2, 50 mg $FeCl_3 \cdot 6H_2O$ and 50 mg $Ni(CH_3COO)_2 \cdot 4H_2O$ in a mortar and placing them in a tube furnace with argon gas, and calcining them at 800 ℃ for 3 h at a temperature increase rate of 5 ℃/min. FeNi@C was the same, but it was necessary to replace the MOF-5-NH_2 by MOF-5, whereas the NC was produced by calcining MOF-5-NH_2 directly in tube furnace.The MOF-derived carbon nanomaterials were synthesized with a high reproducibility, with FeNi@NC retaining about 25% of its initial mass after

Please do not adjust margins

Please do not adjust margins

carbonization at 800 °C.

2 Apparatus and Physical Measurement.

2.1 General Instruments.

Scanning electron microscopy (SEM) data were acquired on a JSM-6700F field emission scanning electron microscope at 10 kV. High resolution transmission electron microscopy (HR-TEM) was acquired on a JEOL JEM2100F microscope at a high voltage of 200 kV. Powder X-ray diffraction patterns (PXRD) were obtained on a Bruker D8 Advance type instrument using Cu Kα radiation (0.154 nm). Fourier Transform Infrared (FT-IR) spectra were obtained using a PerkinElmer Frontier MIR type spectrometer. Fluorescence emission spectra were determined immediately after excitation at 332 nm using an F-7100 spectrofluorometer (Hitachi, Japan). Specific surface area was calculated from nitrogen adsorption data with a relative range (P/P_0) of 0.04-0.2 by the Brunner-Emmett-Taylor (BET) equation. Pore size distribution (PSD) plots were derived from the adsorption and desorption branches of the isotherms according to the Barrett-JoynerHalenda (BJH) model and/or the Horvath-Kawazoe (H-K) model. X-ray photoelectron spectroscopy (XPS) characterisation was carried out on a high-resolution electron energy analyser (Gamma data-Scienta SES The X-ray photoelectron spectroscopy (XPS) characterisation was performed on a high resolution electron energy analyser (Gamma data-Scienta SES 2002) using monochromatic Al Kα X-rays.

2.2 Electrochemical Characterizations.

All electrochemical data were collected via the CHI760E and/or Autolab electrochemical workstation. OER measurements were performed in 1.0 M KOH solution using a typical three-electrode system, the GCE (glassy carbon electrons) with catalyst ink, platinum mesh, and Hg/Hg_2Cl_2 electrode as the working electrode, counter electrode, and reference electrode, respectively. At the same time, we chose Hg/Hg_2Cl_2 as the reference electrode to ensure accuracy and reproducibility in alkaline media. All electrochemical tests in our work were performed without iR correction. We dispersed 2.5 mg of target powder with 12.5 μL of Nafion (5%), 100

Please do not adjust margins

Please do not adjust margins

μL of DI H_2O, and 150 μL of ethanol, and then sonicated it for 1 h. 6 μL of the catalyst ink was then dropped on the surface of the GCE electrode and dried at ambient conditions for 8-10 min. Cyclic voltammograms (CVs) were carried out at a scan rate of 50 mV s^{-1}. Simultaneously, linear scanning voltammetry (LSV) was recorded at a scan rate of 5 mV s^{-1} and electrochemical impedance spectroscopy (EIS) measurements were carried out at a frequency range of 10^5 to 10^{-1} Hz at 1.075 V (*vs.* RHE). The electrochemical double layer capacitance (C_{dl}) curves of the different samples were measured by CV in the non-Faraday region (1.05-1.15 V *vs.* RHE) at different scan rates of 20, 40, 60, 80 and 120 mV s^{-1}. For RRDE (rotating ring disc electrode), the prepared sample ink was also coated onto the glassy carbon disc electrode of RRDE. In order to determine the electron transfer number (N), we utilised the polarisation curve in a 1.0 M O_2 saturated KOH electrolyte at 1600 rpm with a rotational speed of 2.0 mV s^{-1} and an annulus potential of 1.5 V (relative to the RHE): $E_{RHE}=E_{Hg/Hg2Cl2}+(0.059*pH)+0.245$, and the overpotential (η) was calculated using the following formula: η=E(V *vs.* RHE)-1.23 based on the O_2/H_2O equilibrium (1.23 V *vs.* RHE). According to the Tafel equation, the Tafel slope is transferred as follows: $\eta=b-\log(j/j_0)$. The value of the number of electrons transferred (N) can be calculated from the ring and disc currents measured at a rotating ring-disc electrode (RRDE) (size 5.0 mm, geometric surface area 0.196 cm^2; Paine Research Instruments, USA) using the following formula: $N=4-I_d/(I_d+I_r/N_c)$. The disc electrode was cathodically scanned at a rate of 5 mV s^{-1} with the ring potential held at 1.0 V (relative to the RHE). where N is the current collection efficiency of the platinum ring in the RRDE (N = 0.4), and I_r and I_d are the ring and disc currents, respectively.

Simulation Details

In this work, the projector augmented wave (PAW) method to model the valence electron-ion interactions is employed for all calculations. We use periodic (100) slab models consisting of four metal-oxygen layers with three metal sites per layer, which has been considered as the OER active surface in similar oxide models. The slabs are separated by a 15 Å vacuum region and the atomic positions of top two layers are optimized while other two layers are fixed at the optimized bulk position. The Γ-

Please do not adjust margins

Please do not adjust margins

centered (3×3×1) Monkhorst-Pack K-point grids and a plane-wave energy cutoff of 400 eV are used for the slab calculations. In addition, the vibrational frequencies are computed to include the zero-point energies, enthalpy, and entropy to ultimately calculate the free energies at room temperature (298.15 K). The heterojunction with $FeNi_3$ is built on the (110) plane.

Please do not adjust margins

Crystal Data

Table S1. Summary of Crystal Data and Refinement Results for **MOF-5**.

Items	**MOF-5**
Formula	$C_{24}H_{12}O_{13}Zn_4$
Mass	769.90
crystal system	Cubic
Space group	$Fm\bar{3}m(225)$
a(Å)	25.8919(4)
b(Å)	25.8919(4)
c(Å)	25.8919(4)
α(°)	90.00
β(°)	90.00
γ(°)	90.00
V(Å^3)	17357.7(5)
T(K)	100(2)
Z	8
F(000)	3040
R_{int}	0.0488
$R_1(I>2\sigma(I))$	0.1875
wR_2(all reflections)	0.2223

Ref.[1]: For more details on the crystal structure data, please see the previously published works, e.g. The Journal of Physical Chemistry C, 2010, 114, 16181-16186.

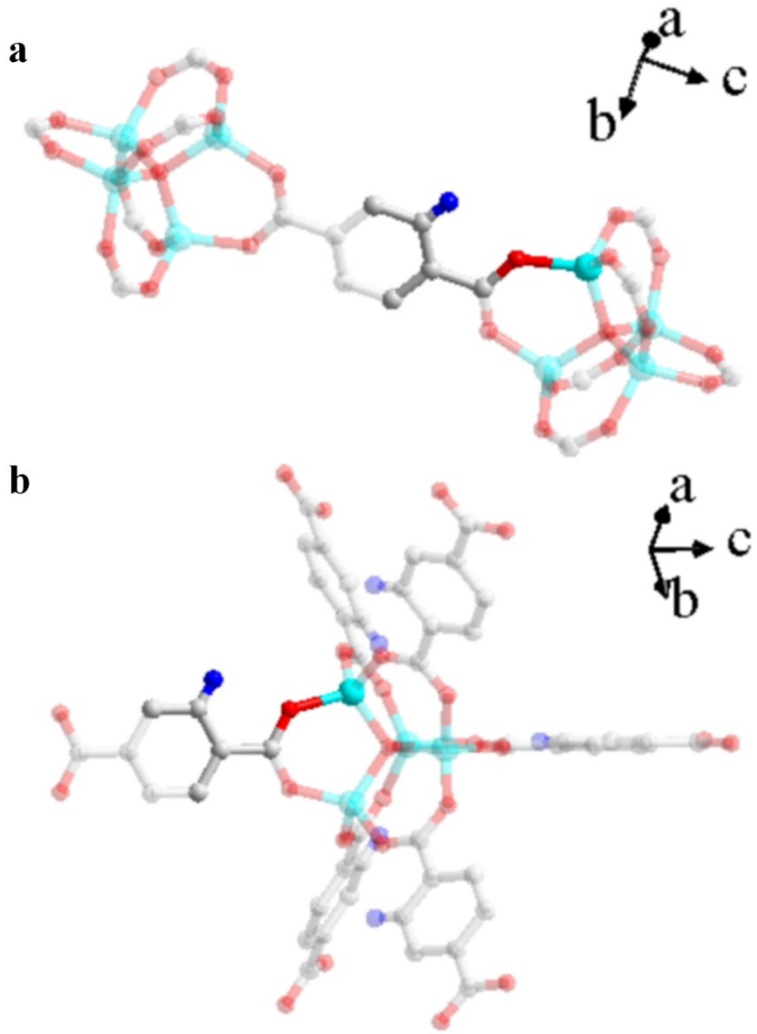

Figure S1. a) Coordination environment of deprotonated ligand in MOF-5-NH_2; b) Coordination environment of Zn_4O SBU in MOF-5-NH_2.

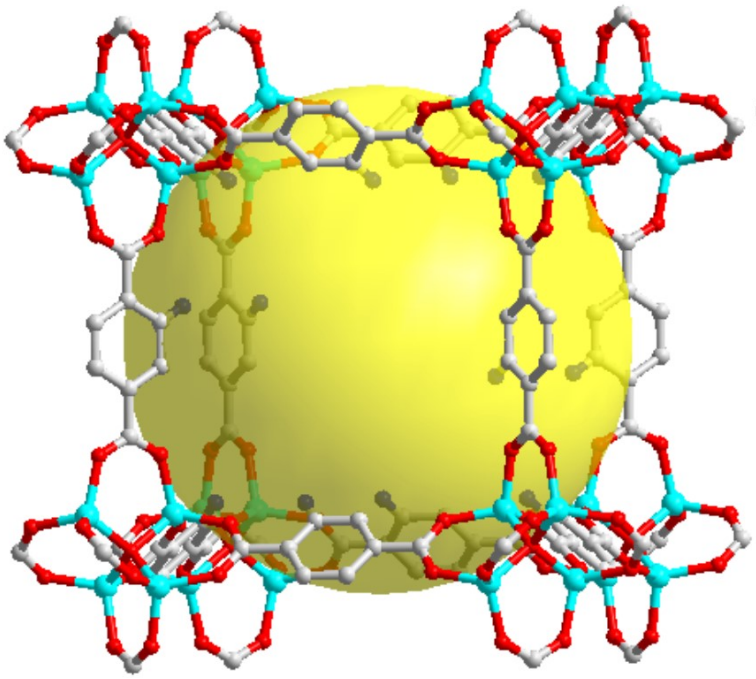

Figure S2. The unit cell and structural components of typical MOF-5-NH_2.

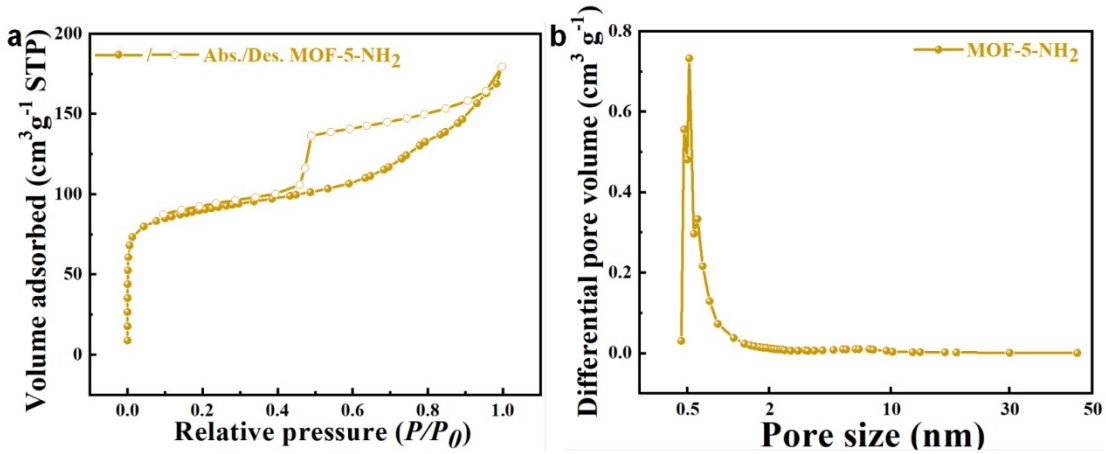

Figure S3. a) N_2 isotherms of MOF-5-NH_2; b) Pore size distribution analysis of MOF-5-NH_2.

SEM/TEM Images

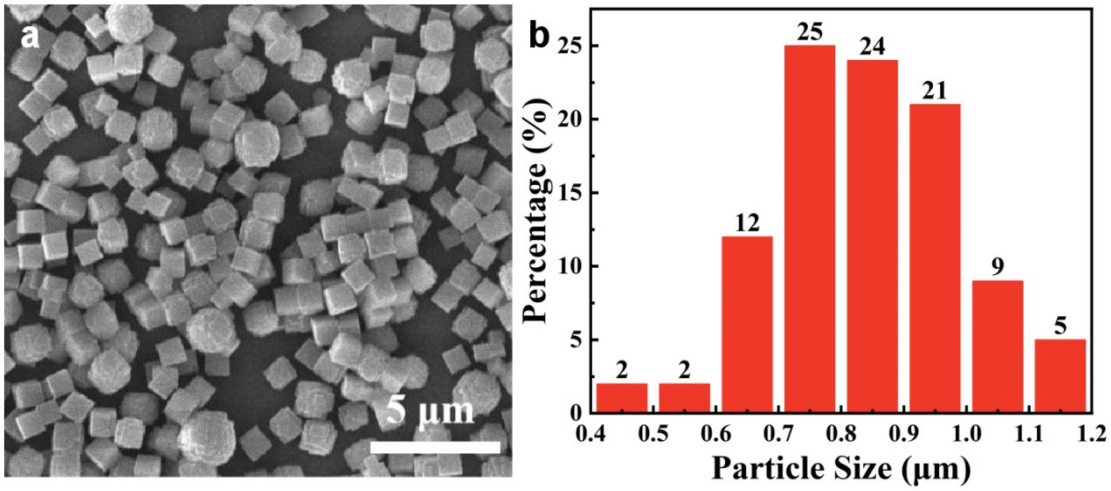

Figure S4. a) SEM images of MOF-5-NH_2; b) Particle size distribution of MOF-5-NH_2.

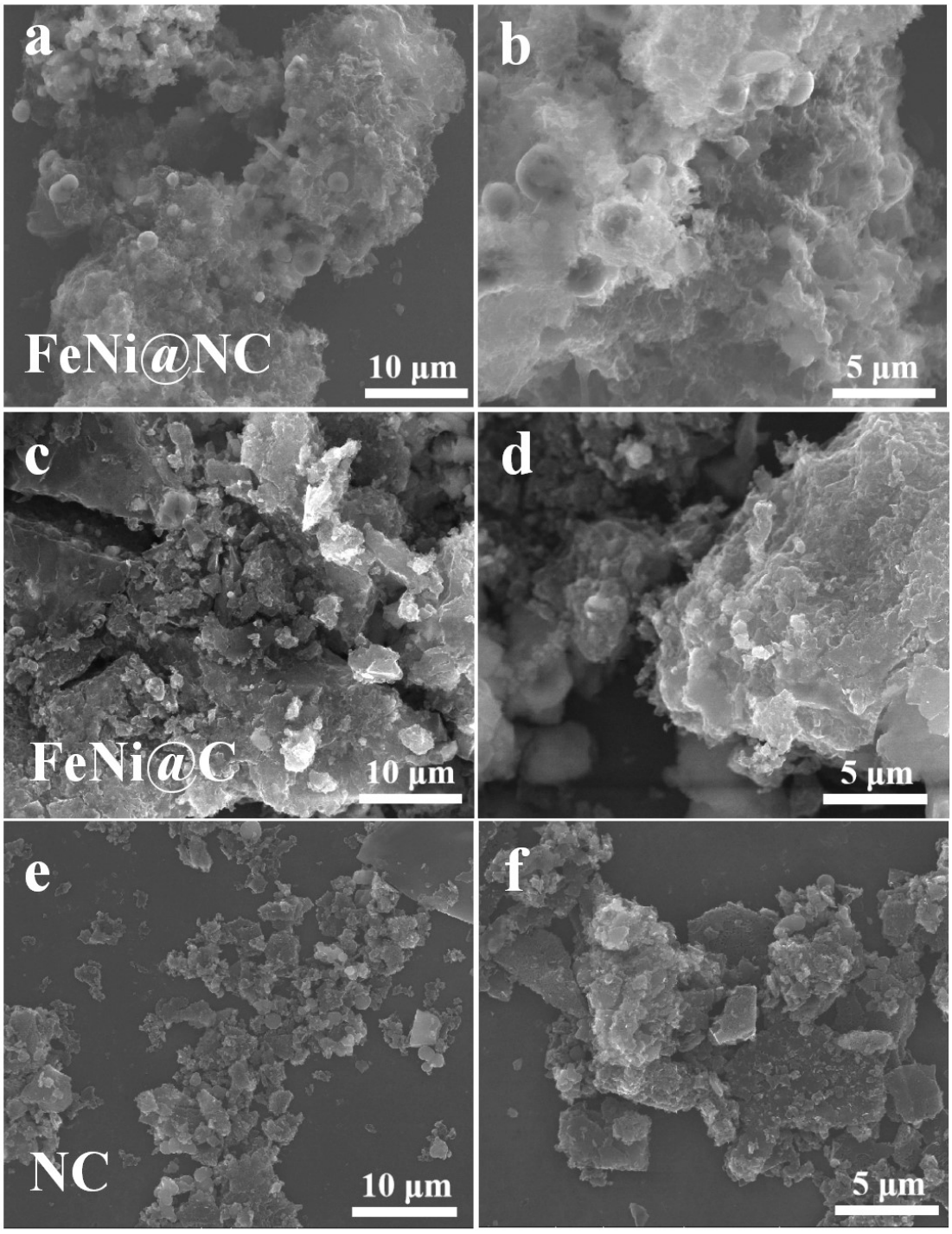

Figure S5. SEM images of a-b) FeNi@NC; c-d) FeNi@C; e-f) NC.

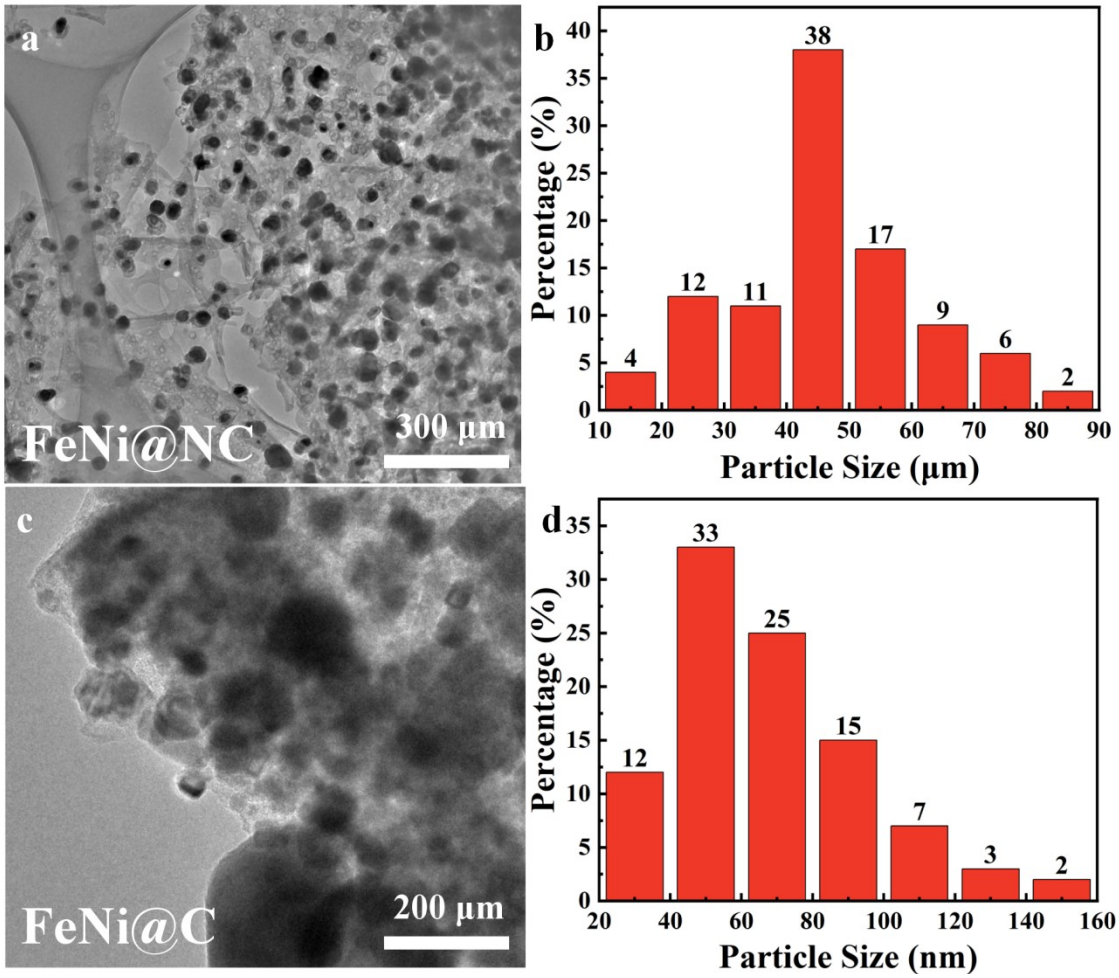

Figure S6. a) TEM image of FeNi@NC; b) Particle size distribution of FeNi@NC;c) TEM image of FeNi@C; d) Particle size distribution of FeNi@C.

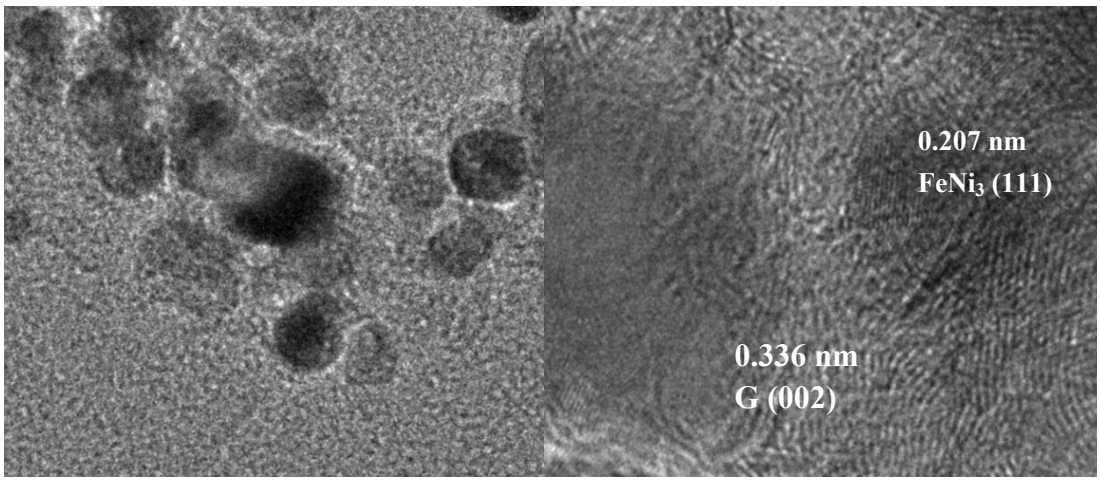

Figure S7. TEM and HR-TEM images of MOF-5-NH_2 derived FeNi@NC.

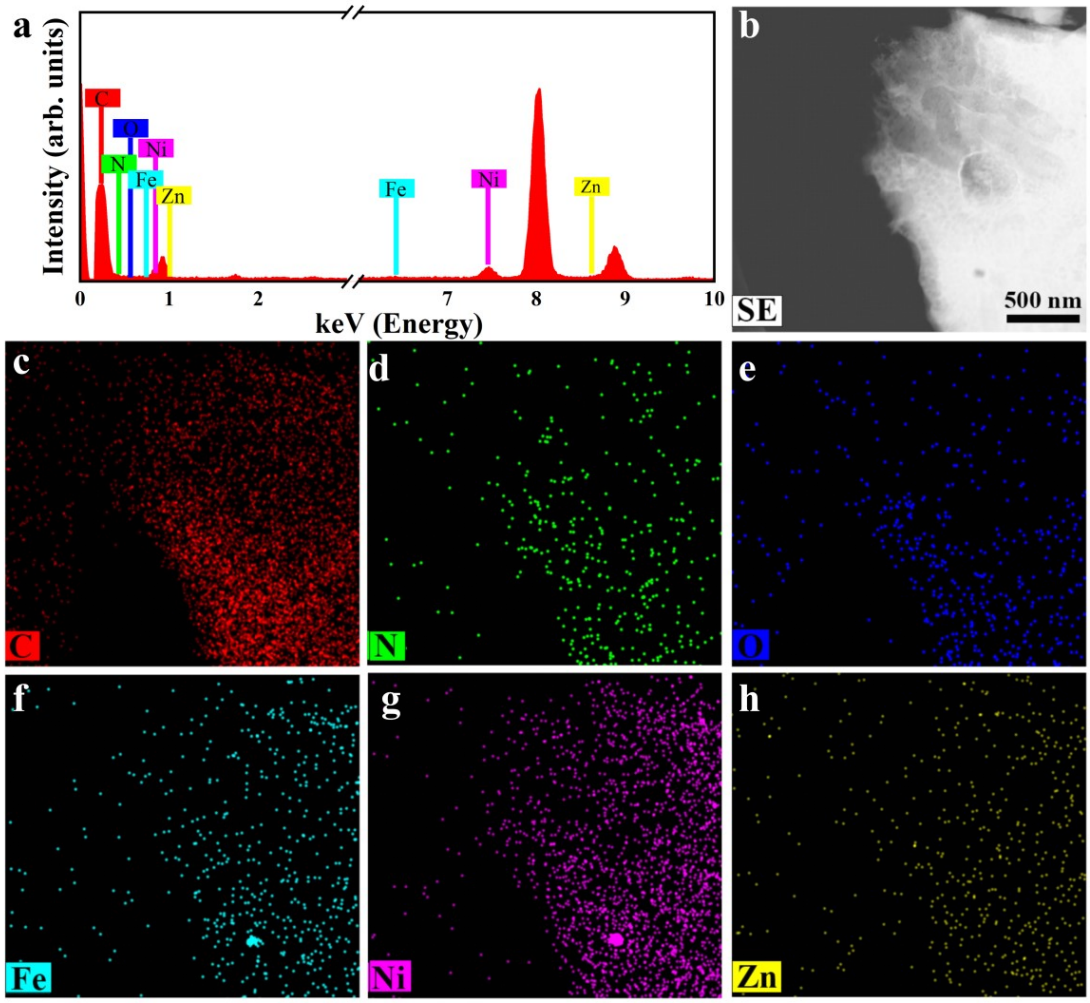

Figure S8. a) The EDS pattern. b-h) HAADF-STEM and element mapping images of FeNi@NC.

The HAADF-STEM image and its elemental mappings further verify the even distribution of Ni, Fe, C, N, O as well as small amount of unremoved Zn elements in FeNi@NC.

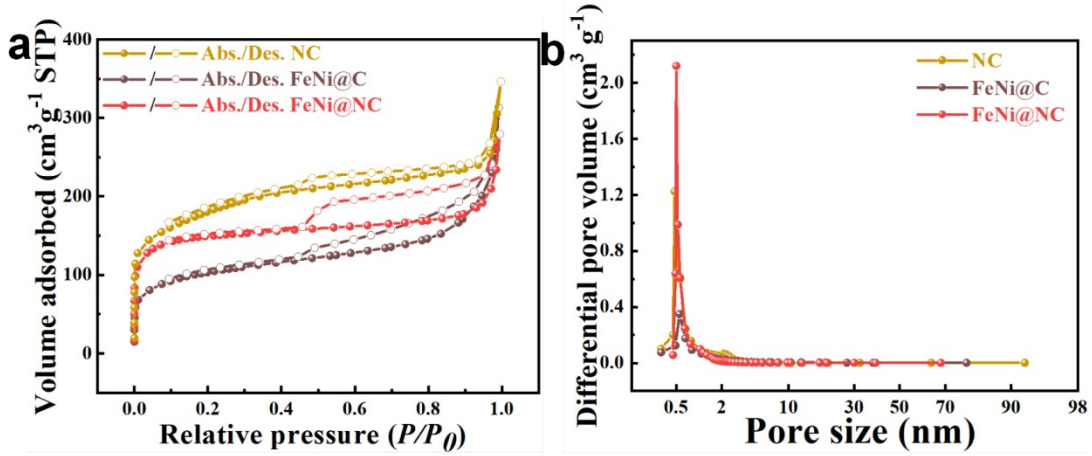

Figure S9. a) N_2 isotherms, b) Pore size distribution analysis of FeNi@NC, FeNi@C, NC.

XPS Data

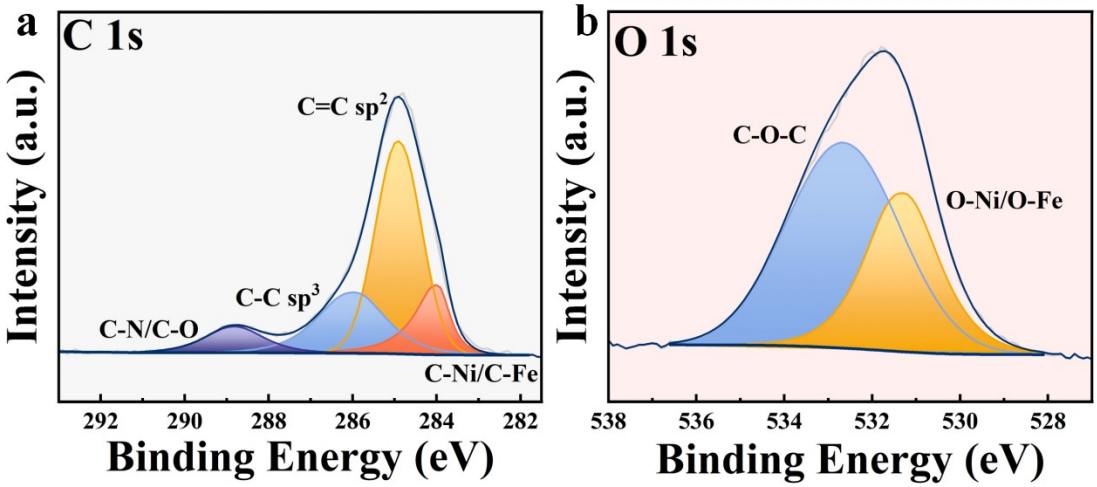

Figure S10. The deconvoluted spectra of a) C 1s; b) O 1s for FeNi@NC.

The high-resolution C 1s spectrum can be fitted to four separate peaks located at 283.8, 284.8, 286.2, and 288.8 eV, which are attributed to C-Ni/C-Fe,C=C sp^2, C-C sp^3, and C-N/C-O, respectively.

In addition, two broad peaks at 532.3 and 532.7 eV for O-Ni/O-Fe and C-O-C.

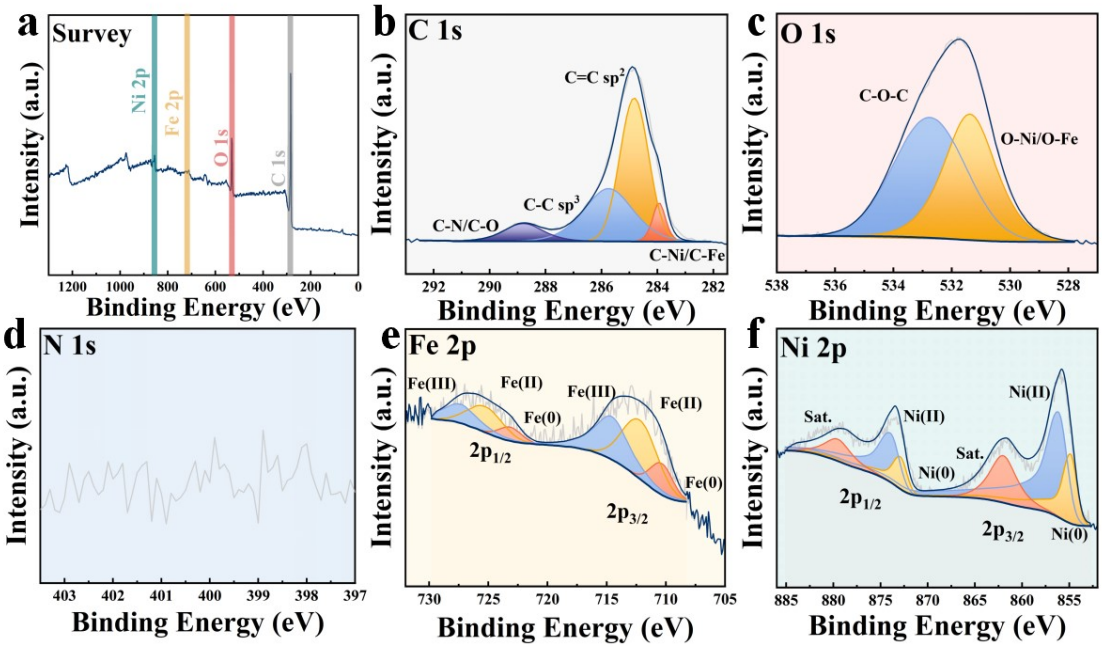

Figure S11. a) The Full XPS spectra of FeNi@C; The deconvoluted spectra of b) C 1s; c) O 1s; d) N 1s; e) Fe 2p; f) Ni 2p.

Electrochemical Data

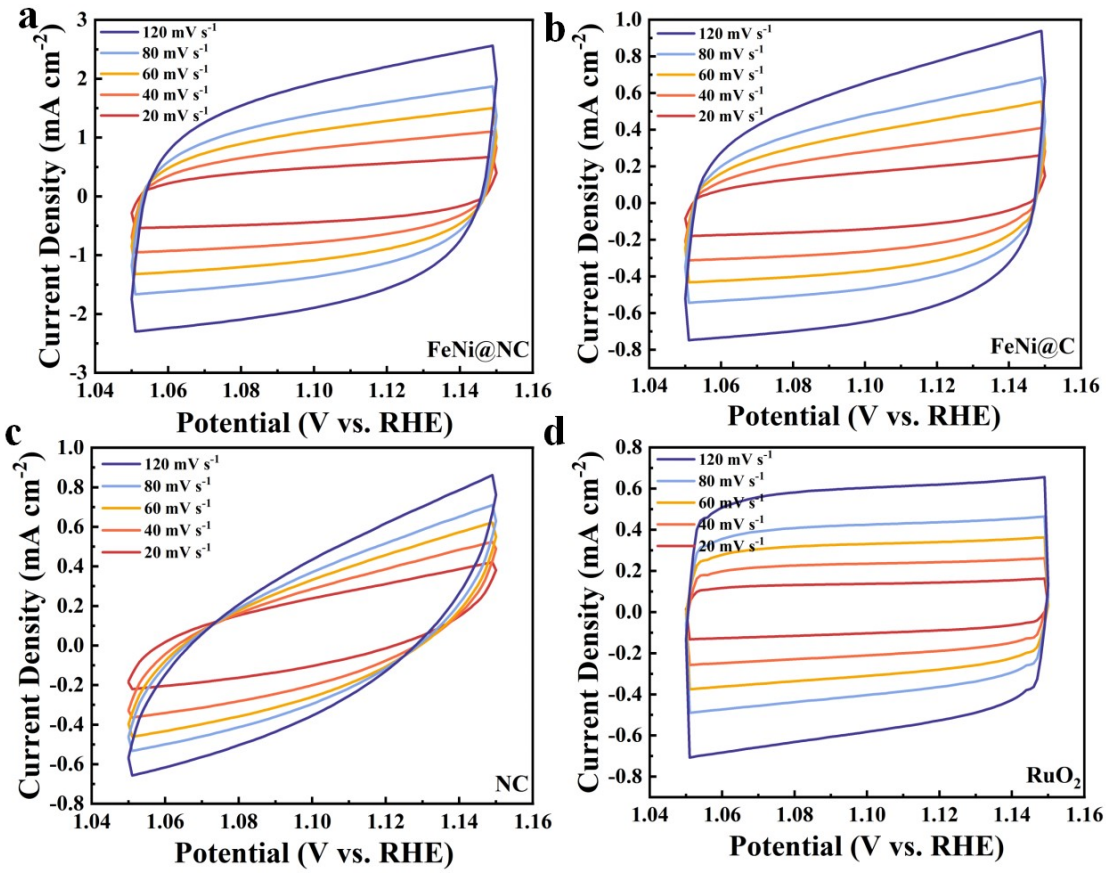

Figure S12. CV curves at different sweep rates from 20 to 120 mV s^{-1} of a) FeNi@NC; b) FeNi@C; c) NC; d) RuO_2.

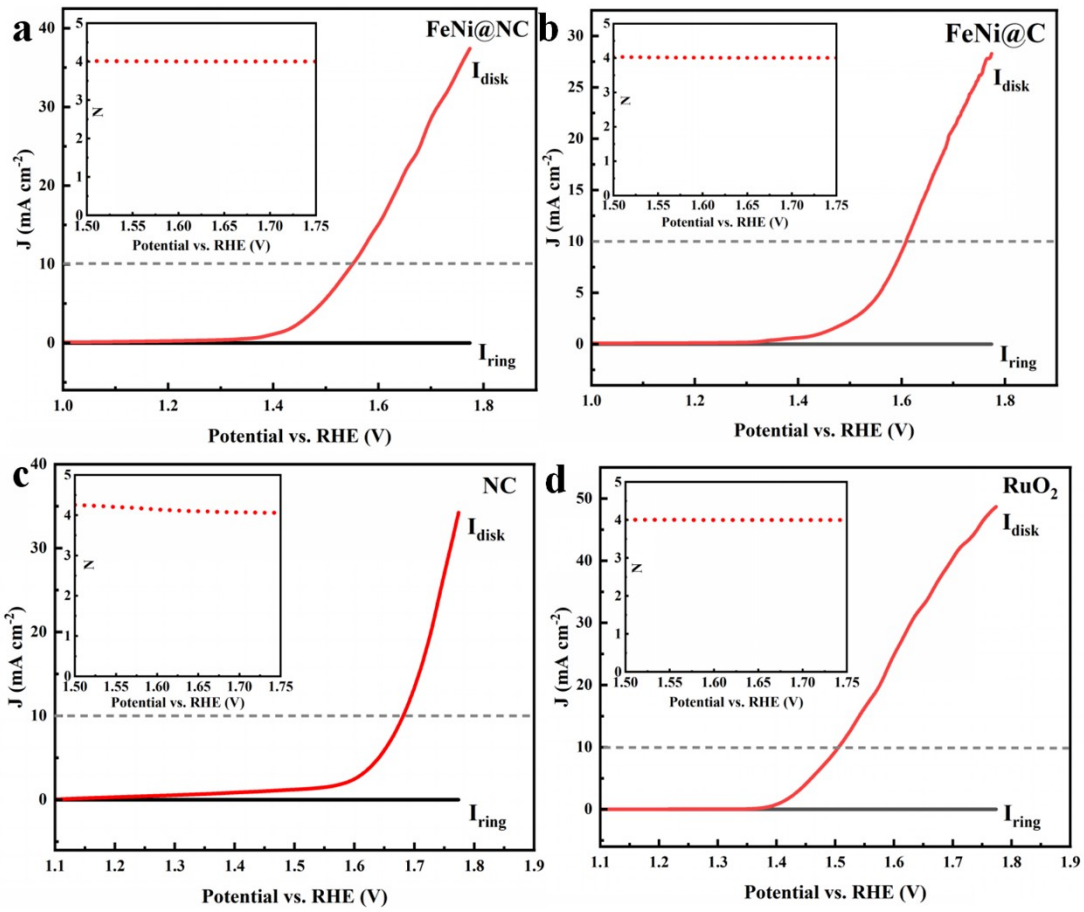

Figure S13. RRDE voltammogram of a) FeNi@NC; b) FeNi@C; c) NC and d) RuO_2 in 1.0 M O_2-saturated KOH electrolyte and its inset shows the corresponding electron transfer number.

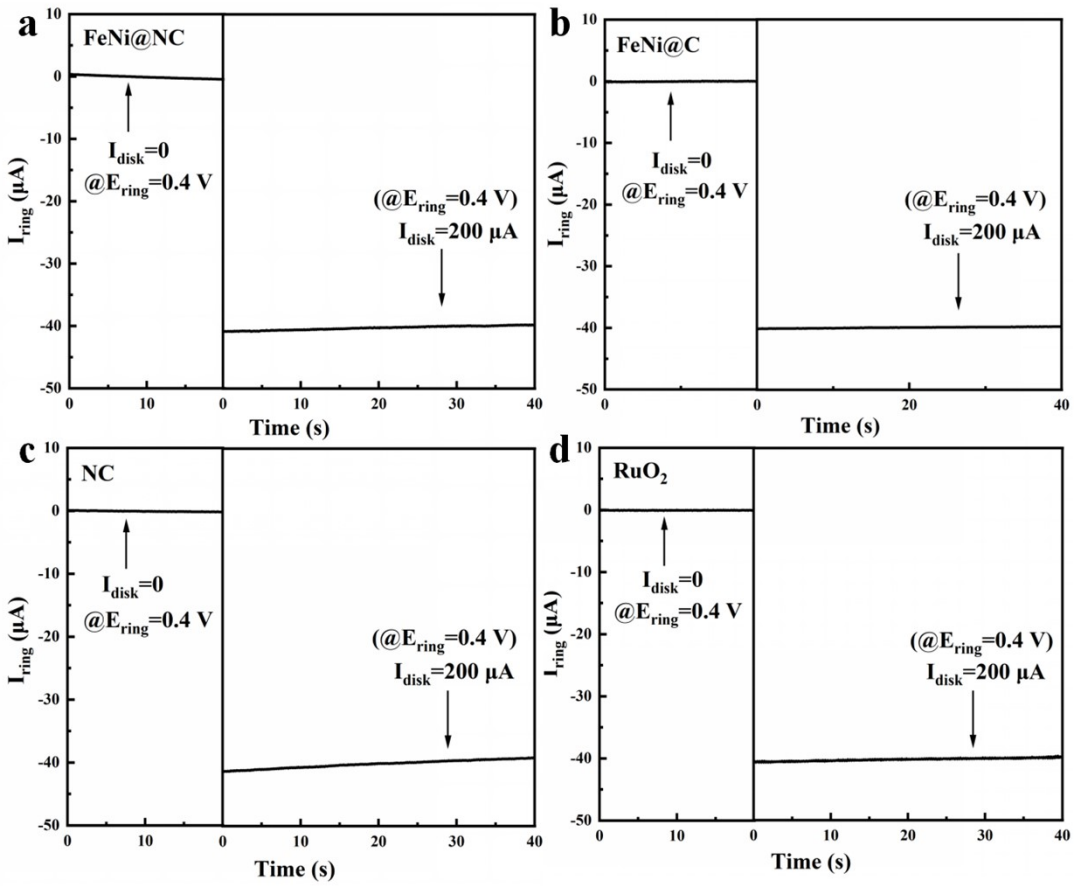

Figure S14. Ring current of a) FeNi@NC, b) FeNi@C, c) NC and d) RuO_2 on an RRDE in 1.0 M N_2-saturated KOH electrolyte.

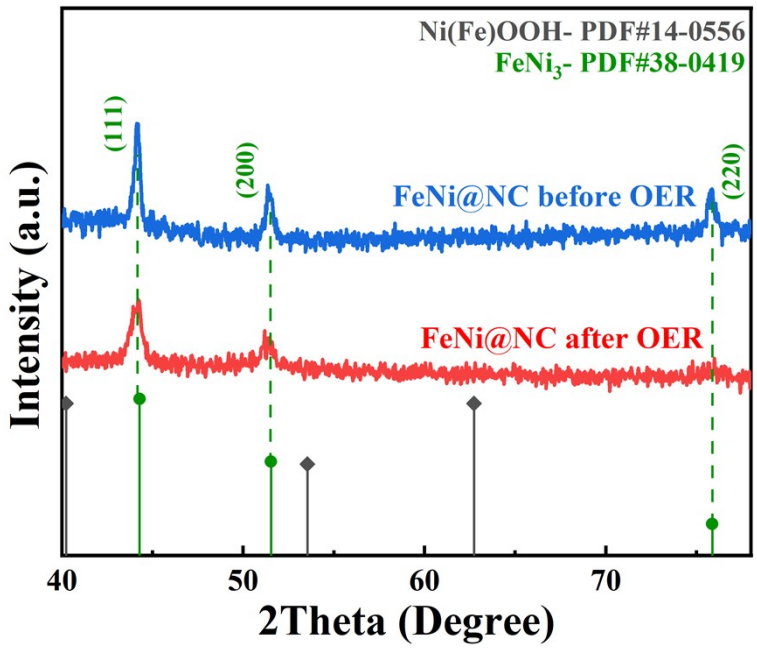

Figure S15. PXRD patterns of FeNi@NC before and after OER.

After the OER, the crystalline $FeNi_3$ phase dose not undergo distinct transformation, but the peak intensity is weakened slightly in the PXRD patterns. Although the diffraction peaks corresponding to Ni(Fe)OOH were not observed, this could be attributed to its low concentration in the material.

Please do not adjust margins

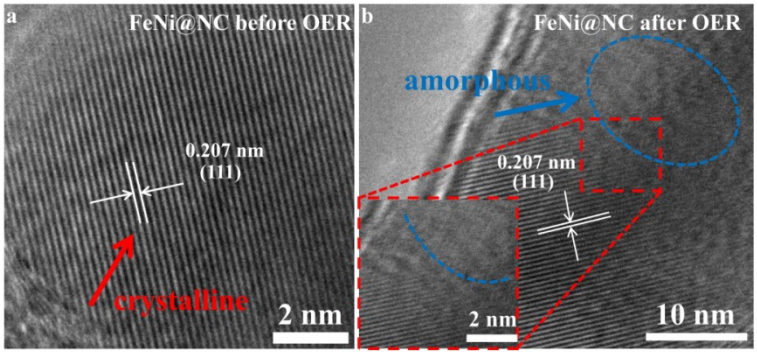

Figure S16. HR-TEM images of FeNi@NC. a) before and b) after OER.

It is evident that lattice streaks associated with $FeNi_3$ particles were clearly visible before the OER test. However, following the OER test, an amorphous substance emerged between the $FeNi_3$ particles and the graphitic carbon layer, suggesting the possible formation of Ni(Fe)OOH.

Please do not adjust margins

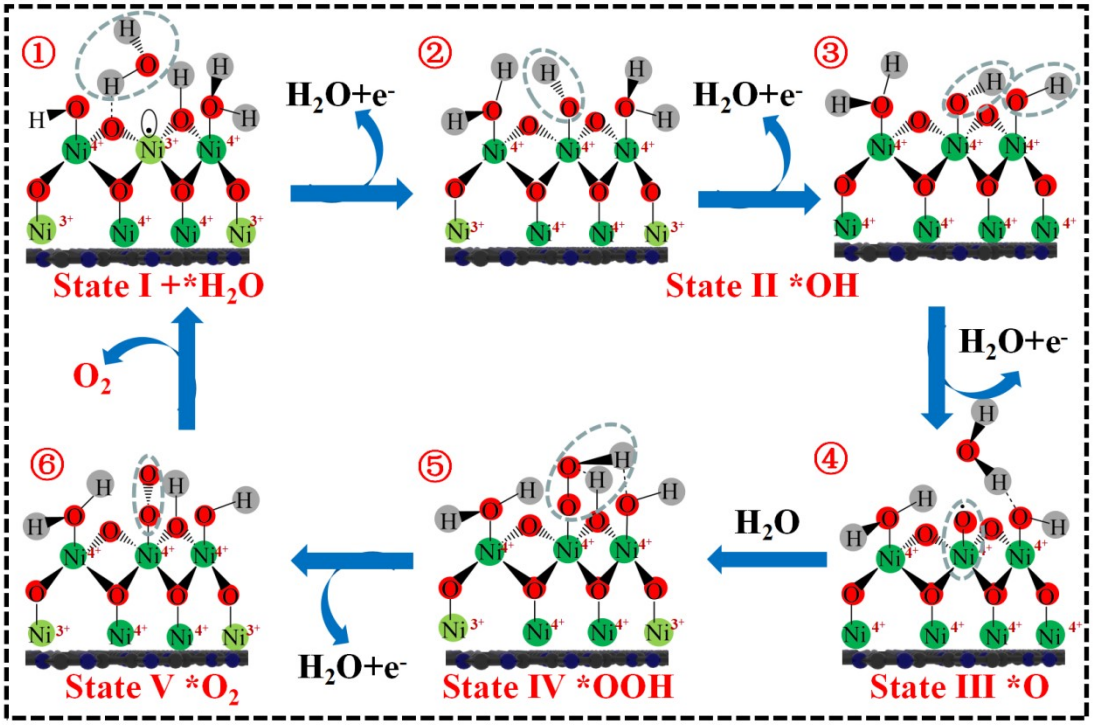

Figure S17. OER mechanism on NiOOH.

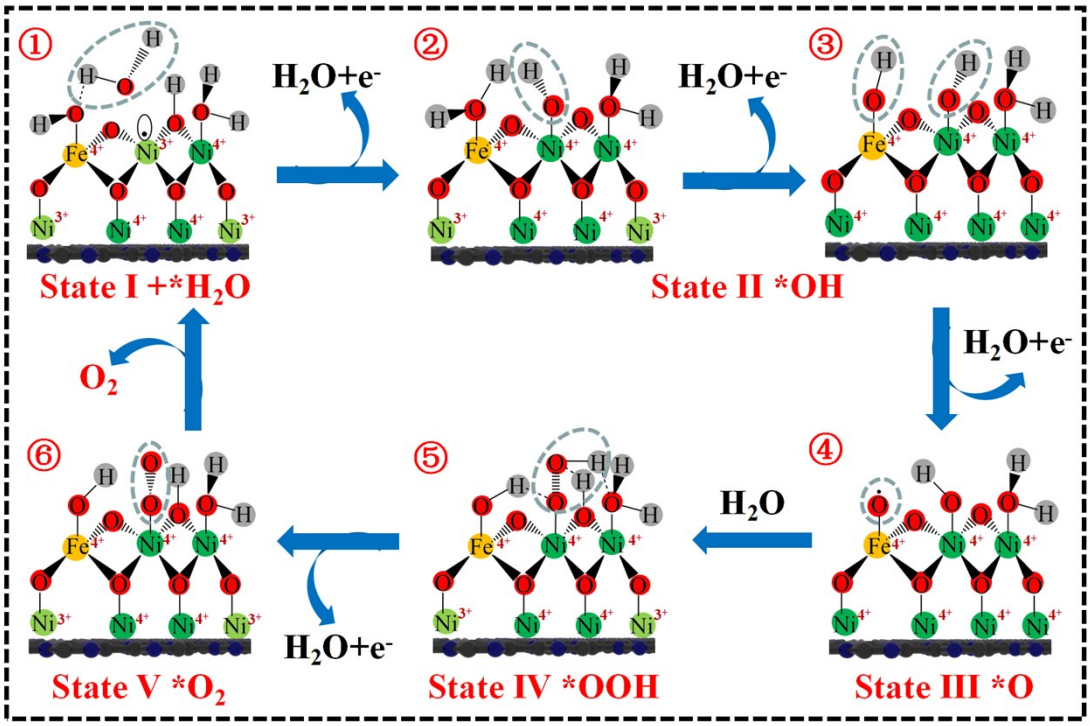

Figure S18. OER mechanism on Ni(Fe)OOH.

In this case, the Ni(Fe)OOH model was selected as an example for detailed interpretation.

First of all, water molecules were attached to the catalyst surface to form $*H_2O$ (State I, ①); after that, an oxidative deprotonation process occurred, leading to the deprotonation on the oxygen between Ni(III) and Ni(IV) and making Ni(III) hydroxylated (State II, ②, $\Delta G_{1\rightarrow2}$ = 1.17 eV), followed by the sequential deprotonation of H_2O adsorbed on the Fe(IV) site by the two protons to give *OH (State III, ③, $\Delta G_{2\rightarrow3}$ = 0.7 eV) and *O (State IV, ④, $\Delta G_{3\rightarrow4}$ = 1.68 eV). The generation of *O is a potentially decisive step in the overall OER process, and compared to NiOOH, Fe doping yields Ni(Fe)OOH containing a high-spin $3d^4$ Fe(IV) active site, which stably generates the unpaired electrons in *O thereby

Please do not adjust margins

reducing the energy required for this step. On the low-spin $3d^6$ Ni(IV), *O combines with H_2O to form *OOH (State V, ⑤, $\Delta G_{4\rightarrow5}$ = 0.01 eV), which is then oxidized on Ni(IV) and adsorbed *OOH is further deprotonated to form $*O_2$ (State VI, ⑥, $\Delta G_{5\rightarrow6}$ = 1.09 eV). Finally, with the dissociation of O_2, the surface state of the catalyst is returned to the State I (⑥, $\Delta G_{6\rightarrow1}$=0.04 eV), reaching the cycle. In conclusion, the doping of Fe effectively reduces the overpotential of the decisive speed step and enhances the OER behaviour.

Please do not adjust margins

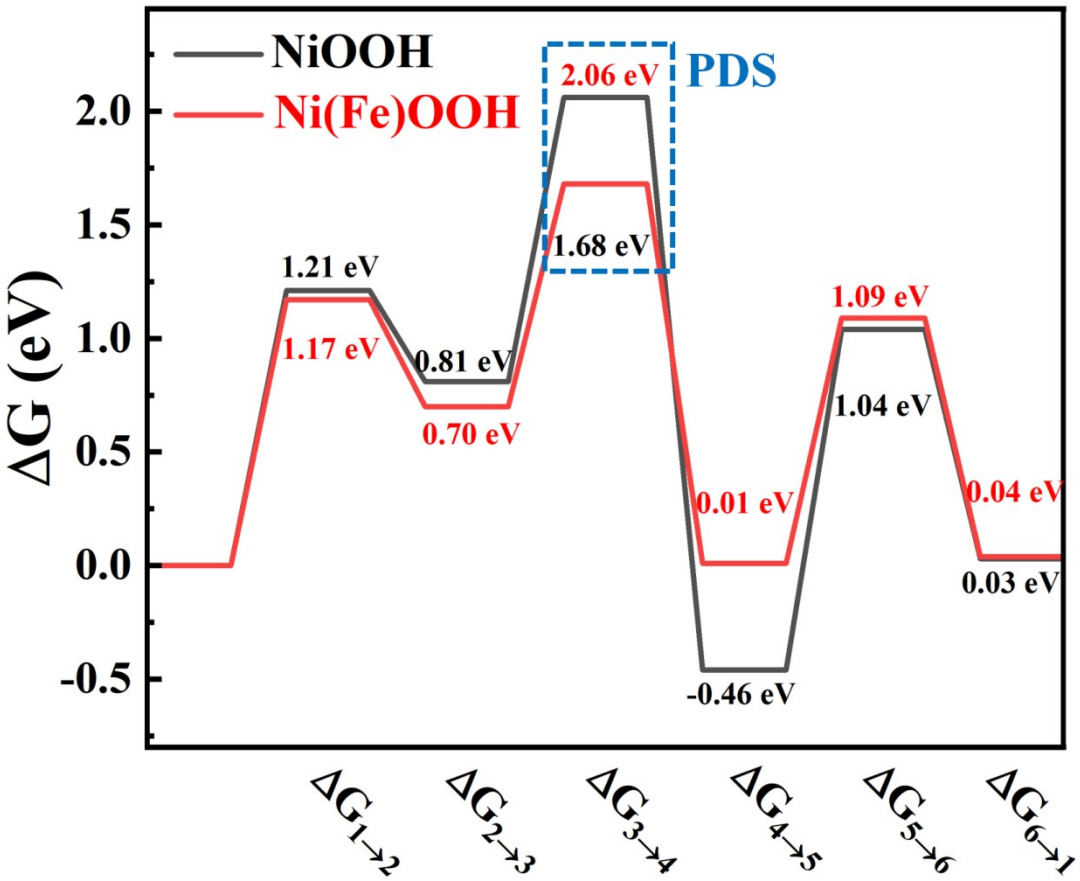

Figure S19. The free energies for NiOOH and Ni(Fe)OOH.

Please do not adjust margins

Additional Tables

Table S2. The BET Surface Area and Total Volume of The Samples by Nitrogen Adsorption and Desorption Measurement.

Samples	**BET surface area (m^2 g^{-1})**	**Total pore volume (cm^3 g^{-1})**
MOF-5-NH_2	285.90	0.2252
FeNi@NC	452.39	0.3619
FeNi@C	337.39	0.4021
NC	590.22	0.4725

Please do not adjust margins

Please do not adjust margins

Table S3. The Composition and Deconvoluted Contents of The Catalysts Based on XPS Measurement.

Samples	Content(%)				
	C	**N**	**O**	**Fe**	**Ni**
FeNi@NC	71.65	3.12	21.62	0.83	2.78
FeNi@C	83.56	--	14.70	0.48	1.26

Please do not adjust margins

Table S4. Electrochemical Parameters of FeNi@NC, FeNi@C, NC, RuO_2.

Samples	**η_{10} (mV)**	**Tafel slope (mV dec^{-1})**	**C_{dl} (mF cm^{-2})**	**R_{ct} (Ω)**
FeNi@NC	306	97.56	14.36	91.2
FeNi@C	334	116.95	4.94	714.1
NC	454	137.71	2.17	1370.2
RuO_2	331	107.11	4.72	183.8

Table S5. OER Performance Comparison between FeNi@NC and Other Electrode Materials.

Samples	**Electrolyte**	**η_{10} (mV)**	**Tafel slope (mV dec^{-1})**	**Reference**
FeNi@NC	**1.0 M KOH**	**306**	**97.6**	**This work**
CoNi1@C	1.0 M KOH	335	55.6	Ref.[2]
Co-CNT/PC	1.0 M KOH	315	73.8	Ref.[3]
FeCoSe@NCNSs	1.0 M KOH	320	95.1	Ref.[4]
FeNiF/NCF	1.0 M KOH	260	67.0	Ref.[5]
Fe-NiO/NF	1.0 M NaOH	305	65.3	Ref.[6]
NP/NiO	1.0 M NaOH	332	65.6	Ref.[7]
CuO-NiO/NF	1.0 M NaOH	319	86.4	Ref.[8]
Ni-MOF@Fe-MOF	1.0 M KOH	265	82.0	Ref.[9]
$Fe_{0.5}$-BMM-10-700	1.0 M KOH	285	79.2	Ref.[10]
Co/CoP	1.0 M KOH	340	79.5	Ref.[11]
Co-P film	1.0 M KOH	345	47.0	Ref.[12]
NiFeC-800-5	1.0 M KOH	269	72.0	Ref.[13]
Co_2P/CNT-900	1.0 M KOH	292	68.0	Ref.[14]
Ag@Co_xP	1.0 M KOH	310	76.4	Ref.[15]
Ni-Fe-P-350	1.0 M KOH	271	53.0	Ref.[16]

Please do not adjust margins

References

1. N. Lock, Y. Wu, M. Christensen, L. J. Cameron, V. K. Peterson, A. J. Bridgeman, C. J. Kepert and B. B. Iversen, *The Journal of Physical Chemistry C*, 2010, **114**, 16181-16186.
2. X. Zhang, J. Luo, K. Wan, D. Plessers, B. Sels, J. Song, L. Chen, T. Zhang, P. Tang, J. R. Morante, J. Arbiol and J. Fransaer, *Journal of Materials Chemistry A*, 2019, **7**, 1616-1628.
3. S. Dou, X. Li, L. Tao, J. Huo and S. Wang, *Chemical Communications*, 2016, **52**, 9727-9730.
4. Y. Pan, M. Wang, M. Li, G. Sun, Y. Chen, Y. Liu, W. Zhu and B. Wang, *Journal of Energy Chemistry*, 2022, **68**, 699-708.
5. M. Zha, C. Pei, Q. Wang, G. Hu and L. Feng, *Journal of Energy Chemistry*, 2020, **47**, 166-171.
6. Z. Qiu, Y. Ma and T. Edvinsson, *Nano Energy*, 2019, **66**, 104118.
7. D. Xiong, C. Lu, C. Chen, J. Wang, Y. Kong, T. Liu, S. Ying and F.-Y. Yi, *Journal of Power Sources*, 2022, **520**, 230884.
8. Z. Wang, J. Ang, B. Zhang, Y. Zhang, X. Y. D. Ma, T. Yan, J. Liu, B. Che, Y. Huang and X. Lu, *Applied Catalysis B: Environmental*, 2019, **254**, 26-36.
9. K. Rui, G. Zhao, Y. Chen, Y. Lin, Q. Zhou, J. Chen, J. Zhu, W. Sun, W. Huang and S. X. Dou, *Advanced Functional Materials*, 2018, **28**, 1801554.
10. S. Xu, Q. Huang, J. Xue, Y. Yang, L. Mao, S. Huang and J. Qian, *Inorganic Chemistry*, 2022, **61**, 8909-8919.
11. Z.-H. Xue, H. Su, Q.-Y. Yu, B. Zhang, H.-H. Wang, X.-H. Li and J.-S. Chen, *Advanced Energy Materials*, 2017, **7**, 1602355.
12. N. Jiang, B. You, M. Sheng and Y. Sun, *Angewandte Chemie International Edition*, 2015, **54**, 6251-6254.
13. J. Ding, Q. Sun, L. Zhong, X. Wang, L. Chai, Q. Li, T.-T. Li, Y. Hu, J. Qian and S. Huang, *Electrochimica Acta*, 2020, **354**, 136716.
14. D. Das and K. K. Nanda, *Nano Energy*, 2016, **30**, 303-311.
15. Y. Hou, Y. Liu, R. Gao, Q. Li, H. Guo, A. Goswami, R. Zboril, M. B. Gawande and X. Zou, *ACS Catalysis*, 2017, **7**, 7038-7042.
16. C. Xuan, J. Wang, W. Xia, Z. Peng, Z. Wu, W. Lei, K. Xia, H. L. Xin and D. Wang, *ACS Applied Materials & Interfaces*, 2017, **9**, 26134-26142.

Please do not adjust margins